Chemical Engineering Journal 160 (2010) 284–292

Contents lists available at ScienceDirect

Chemical Engineering Journal

journal homepage: www.elsevier.com/locate/cej

Quantitative characterizations of long-period fluctuations in a large-diameter bubble column based on point-wise void fraction measurements

Masamori Higuchi[a], Takayuki Saito[b,*]

[a] *Graduate School of Engineering, Shizuoka University, 3-5-1 Johoku, Naka-ku Hamamatsu, Shizuoka 432-8561, Japan*
[b] *Graduate School of Science and Technology, Shizuoka University, 3-5-1 Johoku, Naka-ku Hamamatsu, Shizuoka 432-8561, Japan*

ARTICLE INFO

Article history:
Received 15 October 2009
Received in revised form 28 February 2010
Accepted 4 March 2010

Keywords:
Bubble column reactor
Long-period fluctuation
Bubbly flow
Single bubble-swarm
Optical fiber probe

ABSTRACT

Quantitatively characterizing long-period fluctuations, which reflect the large-scale structure of a bubbly flow in a bubble column reactor, is essential to improving the reactor efficiency. We propose a newly developed method to extract the long-period fluctuations based on point-wise void fraction measurements. The validity of the new method is demonstrated via characterization of long-period fluctuations in a bubble column approximately 400 mm in diameter and 2000 mm in height. First, the characteristics of liquid-phase motion induced by a single bubble-swarm are described based on the results obtained via LDA measurements. The large-scale liquid-phase motion is characterized by an individual bubble cluster (i.e. a region with the same void fraction). We explain the premise of our new method based on these results. Second, we show that the bubbly flows in the bubble column can be divided into three regions (i.e. a time-spatially fluctuated region, a transition region, and a pseudo-homogenous region) based on differences in the distribution patterns of bubble diameters and velocities as well as those between time-series point-wise void fractions obtained from four-point simultaneous measurements. The spatial fluctuations fade out with height from the column bottom. Finally, analyzing the time-series point-wise void fractions measured via four-tip optical-fiber probe (F-TOP), we demonstrate that the long-period fluctuations can be extracted via waveform analysis. The characteristic spectrum pattern also fades out with height. The extracted long-period fluctuations are in good agreement with those obtained from the visualization results for the flows.

1. Introduction

Bubble column reactors and gas lift reactors are widely used in the chemical industry and other industries [1,2] due to their structural simplicity and high-mass-transfer performance. However, due to the extreme complexity of the bubbly flows, details regarding the phenomena occurring in the reactors have remained unclear. Many researchers have been investigating the mass-transfer coefficient in the reactors with regard to the average bubble diameters and average void fractions [3,4]. Furthermore, the flow regimes have been described as functions of the superficial gas velocity and the geometrical properties of bubble columns [5,6].

In order to improve the chemical reactions in bubble column reactors and to establish their similarity rule with regard to scale up, the details of the physical phenomena (i.e. turbulence specification, flow structure, axial dispersion of bubbles, and so on) have been investigated with many experimental approaches. Based on these investigations, the flows can be identified by three specific scales. On the scale of a single bubble, local pseudo-turbulence is induced by the buoyancy current [7]. On an intermediate scale of a single bubble-swarm, the vortical structure, which is characterized by eddies of its surrounding liquid, appears with a size on the order of the bubble-swarm diameter. The vortical structure stirs the liquid phase and radially transports the bubbles. The velocity fluctuation intensity and the integral scale in the liquid phase are modulated by a single bubble-swarm [8]. On a large scale, gravity acts on non-uniformity in the spatial bubble distribution in the bubble mixture. The gravity-driven flow can form results in inhomogeneous bubble distribution, leading to a turbulent flow. Based on observation of the large-scale circulation, the buoyancy-driven bubbly flows remain relatively unstable except in a completely controlled bubble distributor, even if the superficial gas velocity is low [9].

The time-spatial fluctuation above the entrance region generates a coherent structure observed in a large-scale flow. In order to closely approach the essence of the phenomena, we should focus primarily on the fluctuation characteristics of the bubbly flows at comprehensive specific scales.

Over the last decade, several measurement techniques have been carried out to quantitatively observe the characteristics of fluctuation within the bubbly flows.

---

* Corresponding author. Tel.: +81 53 478 1601; fax: +81 53 478 1601.
E-mail address: ttsaito@ipc.shizuoka.ac.jp (T. Saito).

1385-8947/$ – see front matter © 2010 Elsevier B.V. All rights reserved.
doi:10.1016/j.cej.2010.03.012

Nomenclature

$a(t)$	time-series void fraction
A_a	area of a region in Fig. 4
D_{eq}	equivalent bubble diameter (mm)
D_{min}	chord length of minor axis (mm)
D_{maj}	chord length of major axis (mm)
f_{ai}	point-wise void fraction at $(x, y) = (x_i, y_i)$
f_{a1}	point-wise void fraction at $(x, y) = (x_1, y_1)$
F_{a1}	space-average void fraction at $(x, y) = (x_1, y_1)$
T_s	integral time of time-averaged void fraction
V_b	vertical components of bubble velocity (mm/s)
w	vertical components of liquid-phase velocity (mm/s)
φ_1	horizontal angle of bubble contact (°)
φ_2	vertical angle of bubble contact (°)

For instance, ECT (electrical capacitance tomography) has been used to describe the distribution pattern of the gas phase and the time evolution of this pattern [10,11]. Although the macroscopic flow structures and the fluctuation can be well-described based on this measurement technique, the local time-series void fraction cannot be detected at high spatial resolution. Furthermore, in order to improve the numerical schemes for gas–liquid two-phase flows, quantitative understanding of the flows based on experimental results from the small to large-scale physical phenomena is essential.

From these results, we observed the fluctuations of bubbly flow from the perspective of the comprehensive scales by using a point-wise time-series void fraction.

We discuss herein how to extract the long-period fluctuations, which correspond to the large-scale structure of the buoyancy-driven flows, based on point-wise time-series void fractions in the bubble column. Furthermore, using the newly developed method, we characterize long-period fluctuations in a bubble column 400 mm in diameter and 2000 mm in height. First, we consider the relationship between the time-average void fraction and the spatial-average void fraction. Second, characteristics of the liquid-phase motion induced by a single bubble-swarm (i.e. a controlled region with a uniform void fraction) are described based on the results obtained via LDA measurement. The large-scale liquid-phase motion is characterized by the individual bubble cluster (i.e. a region with a uniform void fraction). We explain the premise of our method based on these results. Third, we measured the void fractions, bubble diameters, and velocities in the bubble column using a four-tip optical-fiber probe (F-TOP) [12,13]. We found that the bubbly flows in the bubble column are calcified into three regions (i.e. a time-spatially fluctuated region, a transition region, and a pseudo-homogenous region) based on the distribution patterns of the bubble diameters and velocities. Furthermore, the spatial fluctuations of the void fraction fade out with height from the column bottom. Finally, analyzing time-series point-wise void fractions measured via F-TOP, we demonstrate that long-period fluctuations are well-extracted by applying the newly proposed method. The extracted long-period fluctuations are in good agreement with those obtained from the flow visualization.

2. Experiment

2.1. Buoyancy-driven flows induced by a single bubble-swarm.

The bubble-swarm examined in the present study was generated using a device diagrammed in Fig. 1(a). Nineteen needles (1) (0.32 mm in inner diameter; 0.09 mm in thickness) were arrayed at the bottom of an acrylic water vessel (2) in a lattice-like arrangement, as shown in Fig. 1(b). Two lines supplied pure air from a cylinder (10) to the needle groups of A and B. The flow rate in each line was controlled by micro-control valves (6), respectively. Each line was equipped with a pair of electromagnetic valves, (4), (4′), (5), and (5′), tripped by a digital timer (8). The valve-opening period was 1 ms (i.e. the pure air was injected in this period), and the opening interval was 10 s. The trigger signal was simultaneously inputted to both high-speed video cameras and PC-controlled precision-linear lifts. The fluctuations in bubble diameters launched from the needles were smaller than 0.44 mm (i.e. 2.6% of the average equivalent diameters of 5.44 mm).

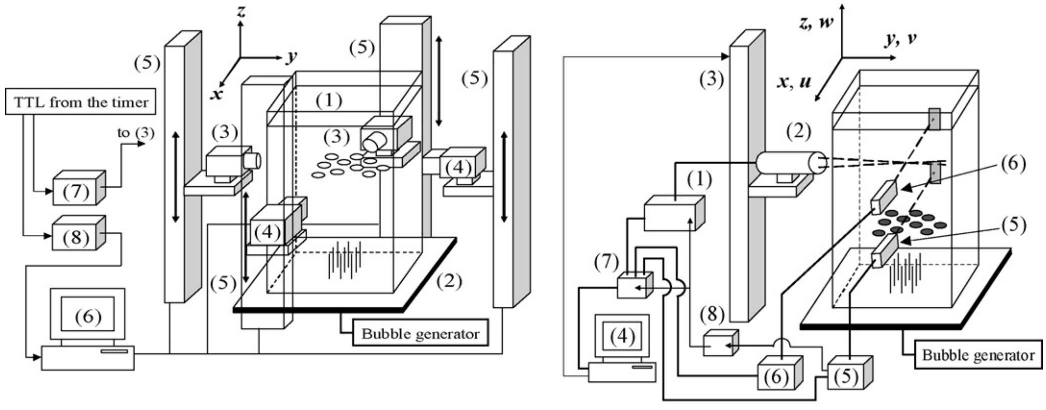

(1) Water vessel, (2) Honeycomb table, (3) High-speed video cameras, (4) Stroboscope, (5) Precision-linear lifts, (6) Control PC, (7) Controllable delay circuit, (8) Controllable delay circuit

(a) For visualizing the motion of a bubble swarm.

(1) LDA system, (2) LDA probe, (3) Automatic 3-axial stage, (4) Control PC, (5) Stroboscope, (6) Laser-optic sensor for the LDA trigger, (7) Laser-optic sensor for detection of a bubble swarm, (8) A/D converter, (9) Controllable delay circuit

(b) For measurement of the liquid-phase motion.

Fig. 1. Experimental setup of a single bubble-swarm. (a) For visualizing the motion of a bubble swarm. (1) Water vessel, (2) honeycomb table, (3) high-speed video-cameras, (4) stroboscope, (5) precision-linear lifts, (6) control PC, (7) controllable delay circuit, (8) controllable delay circuit. (b) For measurement of the liquid-phase motion. (1) LDA system, (2) LDA probe, (3) automatic 3-axial stage, (4) control PC, (5) stroboscope, (6) laser-optic sensor for the LDA trigger, (7) laser-optic sensor for detection of a bubble swarm, (8) A/D converter, (9) controllable delay circuit.

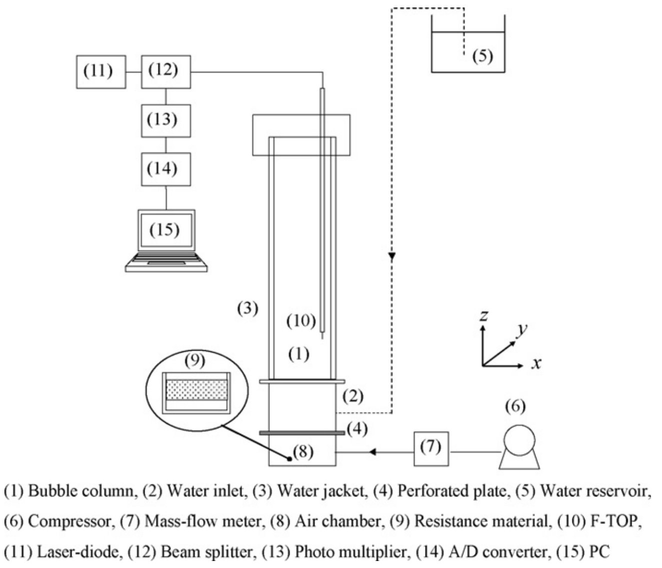

Fig. 2. Experimental setup of bubble column measurement. (1) Bubble column, (2) water inlet, (3) water jacket, (4) perforated plate, (5) water reservoir, (6) compressor, (7) mass-flow meter, (8) air chamber, (9) resistance material, (10) F-TOP, (11) laser-diode, (12) beam splitter, (13) photomultiplier, (14) A/D converter, (15) PC.

2.2. Bubble column

A schematic diagram of the experimental setup employed in the bubble column experiments is shown in Fig. 2. An acrylic bubble column 380 mm in inner diameter and 1500 mm in height is covered with an acrylic water jacket of 440 mm × 440 mm in square cross-section and 1605 mm in height. The bubble column is connected to a steel water inlet 400 mm in diameter and 600 mm in height through a perforated plate (diameter of pores: 1.0 mm; equilateral triangular pitch: 10 mm; the number of pores: 1240). Tap water (temperature 290.5–296 K) is supplied from a water reservoir into the bubble column through the water inlet. Compressed air (temperature 295–296 K), supplied from a compressor, is controlled with a mass flow controller (mass flow rate 67 nL/min) and injected into the air chamber (380 mm in diameter and 200 mm in height).

2.3. Optical fiber probe

In order to measure equivalent diameters and vertical velocity components of bubbles as well as local time-series void fractions, we used four-tip optical fiber probes (so-called F-TOP). The schematic diagram of the F-TOP measurement system is shown in Fig. 3. The laser beam that was emitted from the laser diode propagated through the optical fiber probe. In contrast, in the case of the top of the optical fiber probe being positioned in water, the laser beam was emitted into the liquid phase from the top due to the small difference in the refraction index between the optical fiber and water. On the other hand, while the top was positioned in air, the laser beam was reflected at the top and then returned back through the same fiber. The optical signal that backed through each fiber was inputted into the photomultiplier through a beam splitter. The output signals from the photomultipliers were stored at PC through an A/D converter.

An outline of the F-TOP is shown in Fig. 4. Every probe is set in a needle 0.23 mm in diameter. Three outer probes (OP_i, i: 1–3) are set at the apexes of an equilateral triangle of 0.45 mm, and their tops are positioned on the same plane. The center probe (CP) is positioned at the center of the triangle. The clearance between the top of the CP and the tops of the OP_i is 2.0 mm.

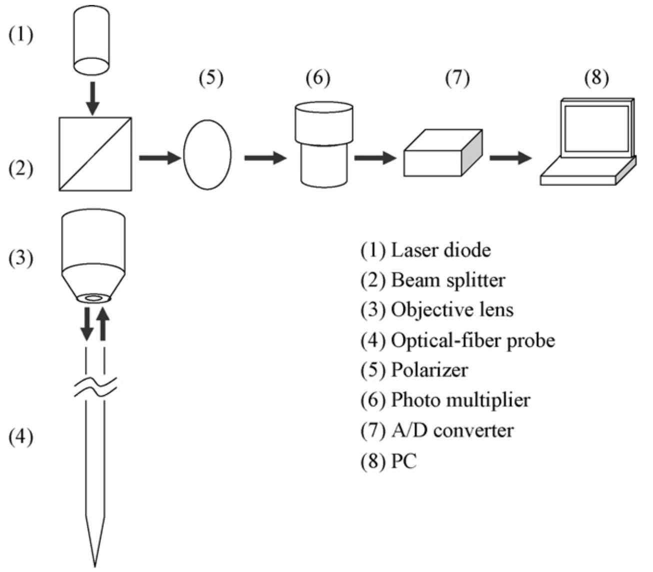

Fig. 3. F-TOP measurement system. (1) Laser diode, (2) beam splitter, (3) objective lens, (4) optical-fiber probe, (5) polarizer, (6) photomultiplier, (7) A/D converter, (8) PC.

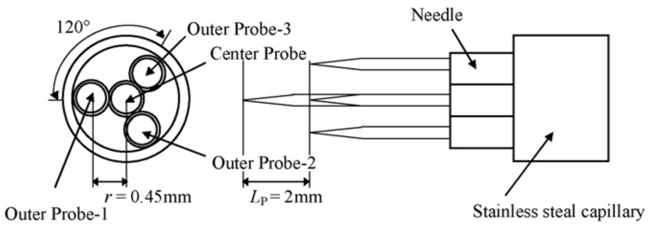

Fig. 4. Structure of F-TOP.

2.4. Processing of F-TOP data

A typical signal of the CP from the photomultiplier is plotted in Fig. 5. First, the output signals of F-TOP are smoothed via a 25-point moving average method. Second, each gas-phase level V_G and liquid-phase level V_L are determined, and two types of thresholds T_{hL} and T_{hH} are determined. Applying the threshold levels to the smoothed signals, intersection points (A)–(D) are detected. In the present study, the high threshold level T_{hH} is 40%, and the low threshold level T_{hL} is 20% of the whole signal amplitude (i.e. V_G–V_L).

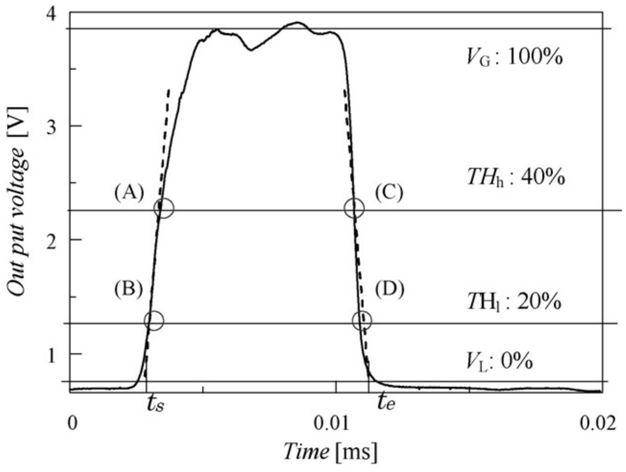

Fig. 5. Typical signal of single optical fiber probe.

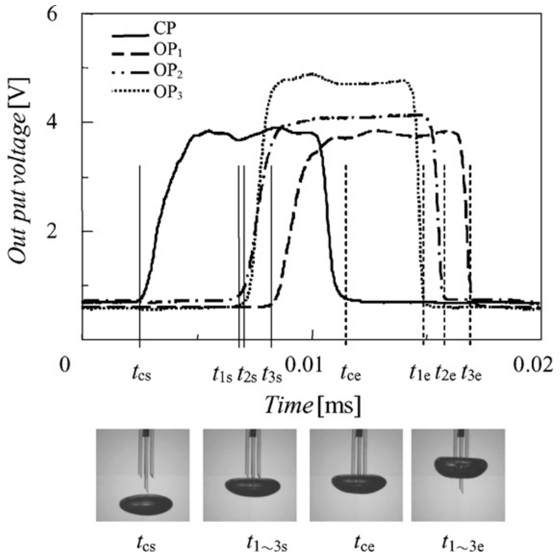

Fig. 6. Typical sample of the set of F-TOP signals and time-series contact process.

Third, t_{ie} and t_{is} (i = c, 1, 2, 3) are calculated; t_s is the time that the top of the probe touches the frontal bubble surface; t_{is} is the time that the top goes through the rear bubble surface.

A typical sample of F-TOP signals is shown in Fig. 6. The equivalent bubble diameter D_{eq} and the vertical velocity component of bubble V_b were calculated by the following equations:

$$V_b = \frac{3L_p}{t_{1s} + t_{2s} + t_{3s} - 3t_{cs}} \tag{1}$$

$$D_{min} = V_b(t_{ce} - t_{cs}) \tag{2}$$

$$D_{maj} = D_{min} r_{axi} \tag{3}$$

$$D_{eq} = \sqrt[3]{D_{maj}^2 D_{min}} \tag{4}$$

First, the minor axis of bubble D_{min} was calculated from the vertical velocity component of bubble V_b and probe clearance L_p. Second, the major axis D_{maj} was determined by referring to an appropriate aspect ratio r_{axi} that was experimentally obtained by Fan and Tsuchiya [14]. Finally, the equivalent bubble diameter D_{eq} was calculated from the bubble volume. Furthermore, intersection angles (φ_1 and φ_2 shown in Fig. 7) between the probe axis and bubble vector were calculated based on this measurement technique.

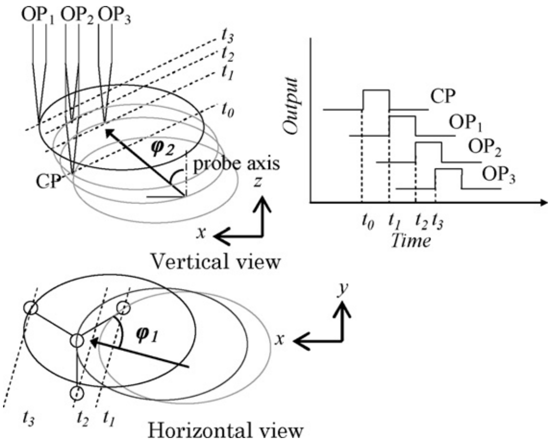

Fig. 7. Relationships between the time that the top of the probe touches the frontal bubble surface t_{is} and intersection angles $\varphi_{1,2}$.

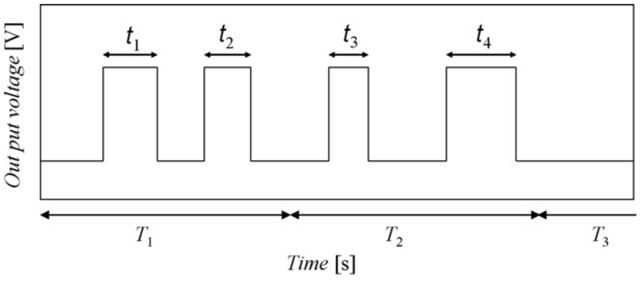

Fig. 8. The outline of time-series raw data of CP.

The angles were calculated by the following equations:

$$\varphi_1(^\circ) = 60\sqrt{\frac{t_3 - t_2}{t_3 - t_1}} \tag{5}$$

$$t_{ave} = \frac{t_1 + t_2 + t_3}{3} \tag{6}$$

$$\varphi_2(^\circ) = \tan^{-1}\sqrt{\frac{(t_{ave} - t_1) + (t_3 - t_{ave}) + (t_3 - t_1)}{3(t_{ave} - t_0)}} \tag{7}$$

When $\varphi_1 < 0^\circ$, $\varphi_1 > 45^\circ$, the calculation results of the bubble velocities and diameters show a decrease in accuracy. Therefore, in these cases, the calculation results are automatically rejected [2].

2.5. Local time-series void fraction

The outline of the time-series raw data is shown in Fig. 8. A summation value of the time interval t_j was calculated at each average time T_i: t_i is the interval of time that the top of the center probe existed in the gas phase. The local time-series void fraction $a(t)$ was calculated by the following equation:

$$a(t) = \frac{\sum_{j=1}^{m} t_j}{T_i} \quad (i = 0, 1, 2, \ldots, n) \tag{8}$$

2.6. Processing of LDA data

In applying LDA to bubbly flow measurements, scattering laser-light noises are inevitably sampled. Considering that the number of bubbles was very small (only 38 bubbles) in the present study, a data-processing method utilizing the triple-peak Laser–Doppler technique [15] has been newly developed.

A typical signal in measuring the surrounding liquid of a bubble is shown in Fig. 9. Triple peaks are observed; Peak-A, Peak-B, and Peak-C correspond to the focus-bubble positional relationships: i.e. frontal bubble Doppler burst, scattering bubble noise, and rear bubble Doppler burst, respectively. The signal usually lacks Peak-A and/or Peak-C. The sequence of data processing is summarized in Fig. 10. This sequence consists of five processes: (1) smoothing of raw data; (2) calculating the threshold level for detecting Peak-B; (3) calculating the threshold levels for detecting the desired Doppler burst (liquid-phase motion); (4) detecting the Doppler bursts; and (5) converting them to velocities.

In the first process, the raw data (i.e. A/D data from the photomultiplier through an A/D converter) were smoothed using a digital low-pass filter (cut of frequency = 400 Hz); hereafter the processed data is called LPFD. In the second process, the standard deviation of LPFD, σ_0, was calculated. Focusing on the large difference in intensity levels between the spike noise of the scattering bubble noise (SBN) and the Doppler burst signal (DBS), the threshold level for detection of SBN was determined to be $0.095\sigma_0$.

In the third process, the threshold levels for detection of DBS were obtained from the iterative process of calculating the standard

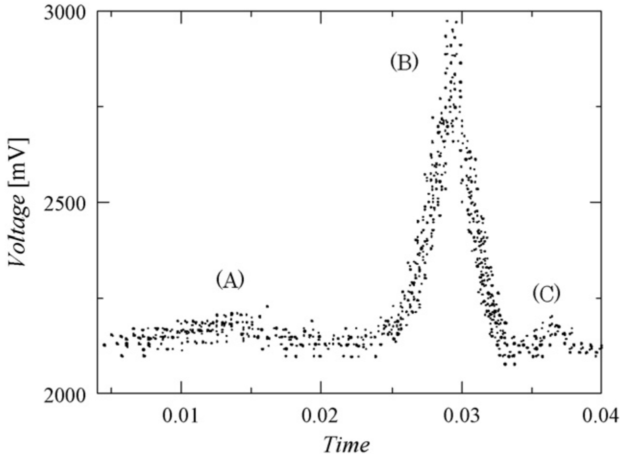

Fig. 9. A typical signal in the measurement of the surrounding liquid of a bubble.

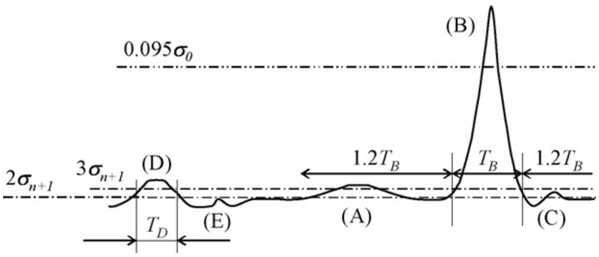

Fig. 11. A typical signal in the measurement of the surrounding liquid of a bubble.

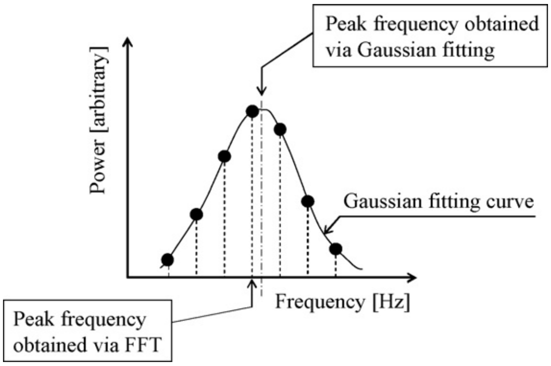

Fig. 12. The FFT results analyzed by the Gaussian curve fitting.

deviation and removing some data based on the standard deviation. Deviations larger than $\pm 3\sigma_0$ were removed from the LPFD, leaving the newly processed dataset NPD_0. The standard deviation σ_i of $\mathrm{NPD}_i - 1$ was then calculated, and deviations larger than $\pm 3\sigma_i$ were removed from $\mathrm{NPD}_i - 1$, leaving the newly processed dataset NPD_i. This process was iterated until $|3\sigma_n - 3\sigma_{n+1}| < 1$, and the threshold levels for detecting DBS, $3\sigma_{n+1}$, and $2\sigma_{n+1}$, were then obtained.

In the fourth process, DBS were detected from NPD_0 using the above threshold levels. Usually, the intensity level of DBS is on the same order as those of the frontal bubble Doppler burst and the rear bubble Doppler burst. Hence, as shown in Fig. 11, DBS detected in the time interval of $1.2T_\mathrm{B}$ before and after SBN was considered to be FBDB and RBDB, and it was removed, with T_B corresponding to the duration of SBN. The DBS_S finally detected were processed via FFT. The FFT results were analyzed by Gaussian curve fitting, and the peak frequency of the DBS_S was then obtained, as shown in Fig. 12; furthermore the frequency was converted to the velocity.

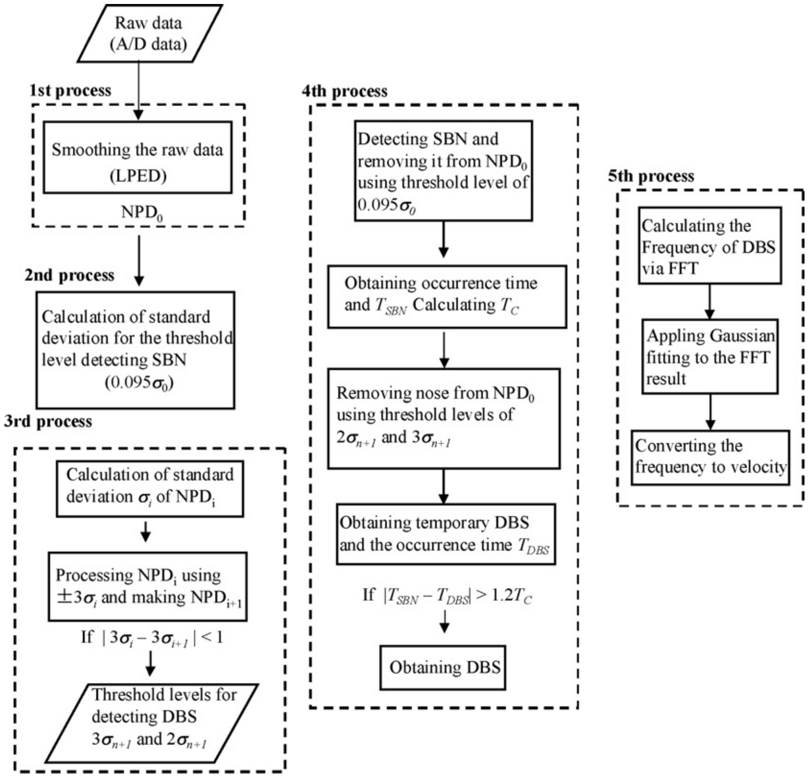

Fig. 10. The sequence of data processing of LDA signal.

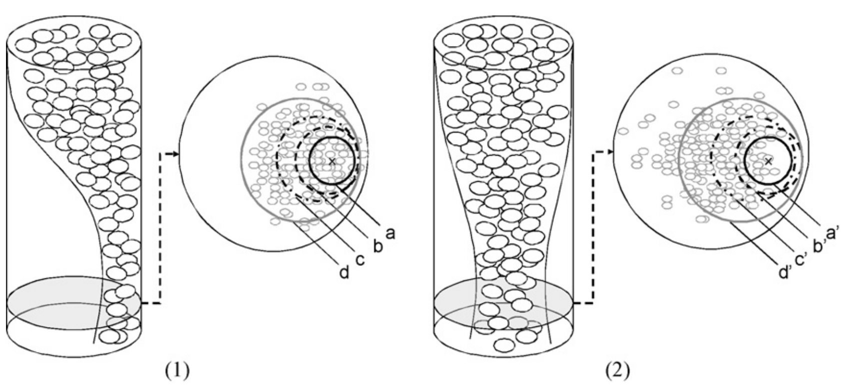

Fig. 13. A model of large-scale (i.e. long-period) fluctuations in a bubble column.

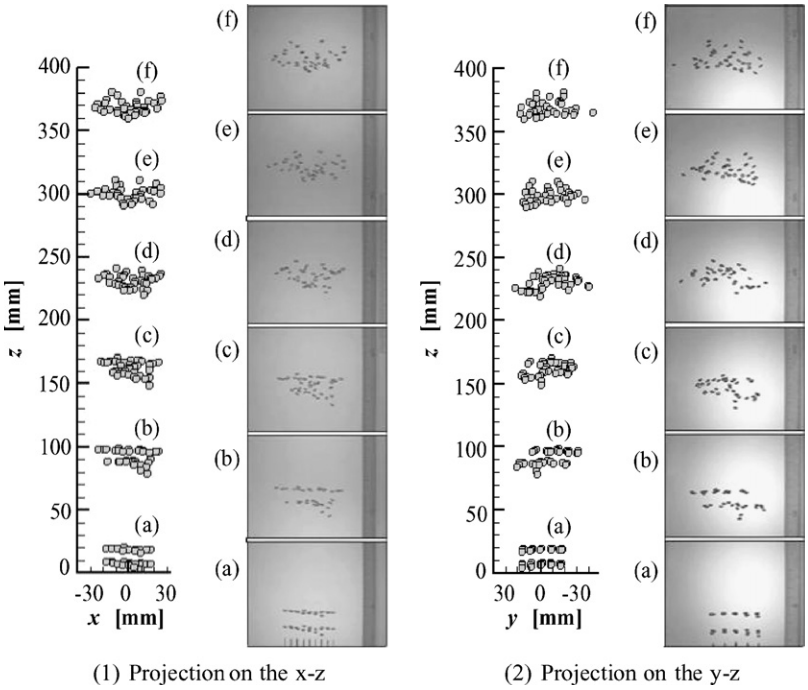

Fig. 14. Typical time evolution of the bubble-swarm. (1) Projection on the *x*–*z* and (2) projection on the *y*–*z*.

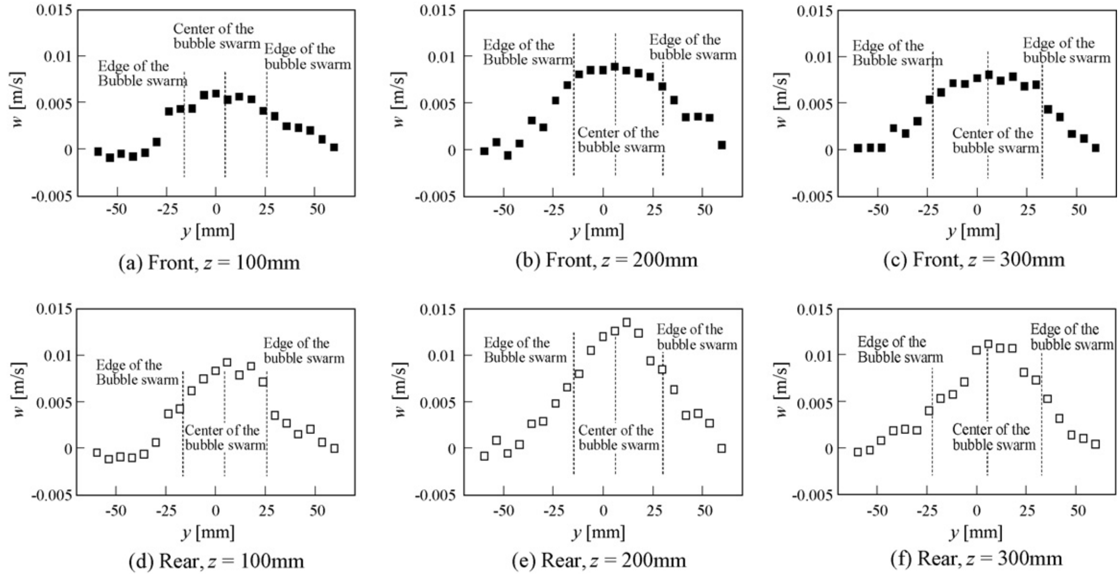

Fig. 15. Profiles of the average of vertical velocity component at the front and rear regions. (a) Front, $z = 100$ mm, (b) front, $z = 200$ mm, (c) front, $z = 300$ mm, (d) rear, $z = 100$ mm, (e) rear, $z = 200$ mm, (f) rear, $z = 300$ mm

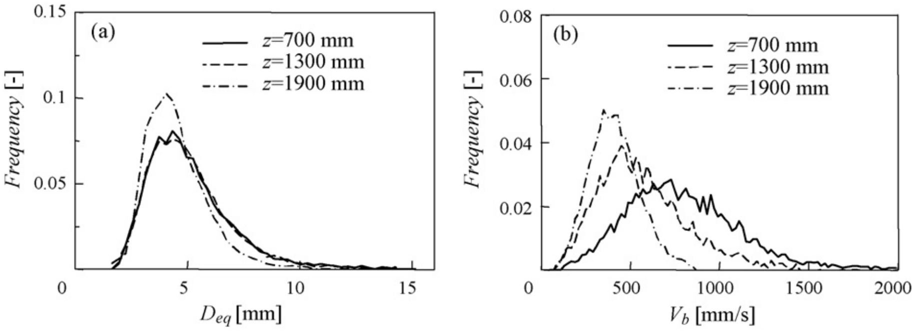

Fig. 16. Statistical distributions of bubble parameter: (a) histograms of equivalent bubble diameter; (b) histograms of vertical components of bubble.

3. Relationship between time-average point-wise and spatial-average void fractions

We considered a method to extract the long-period fluctuations formed in a bubble column based on time-series point-wise void fractions. Fluctuations of the void fractions in time and space are modeled as illustrated in Fig. 13. A point-wise void fraction f_{ai} at (x_i, y_i, t) in the region (a) should have very similar characteristics to those of f_{a1} at (x_1, y_1, t) in the same region (a); i.e. $f_{ai} \approx f_{a1}$. The space-average void fraction at the region (a) $F_a(t)$ is obtained by the following equation:

$$F_a(t) = \frac{\oint_S f(x, y, t)\,dS}{A_a} \tag{9}$$

A_a is the area of region (a). Assuming that $F_a(t)$ is approximated by the time-average of the point-wise void fraction $F_{at}(x_1, y_1)$ at (x_1, y_1) in region (a), $F_a(t)$ can be expressed by

$$F_a(t) = \frac{\oint_S f(x, y, t)\,dS}{A_a} \approx \frac{\int_{t_1}^{t_2} f_a(x, y, t)\,dt}{t_2 - t_1} \tag{10}$$

The larger integral range in time reflects the space-average void fraction in the larger regions (e.g. regions (b), (b′), (c), and (c′)). The space-average void fraction at the larger region reflects some larger organized structure of the bubbly flow. As a result, the time-average point-wise void fraction at (x, y) in an appropriate integral time range indirectly represents the corresponding organized structure.

4. Results and discussion

4.1. Buoyancy-driven flow induced by a single bubble-swarm

Time evolution of a single bubble-swarm. Fig. 14 shows the time evolution of a bubble-swarm projected on the x–z and y–z planes. The later bubbles form a line on a z-plane as well as the preceding bubbles just after being released from the needles. At $z = 29$ mm, the later bubbles begin to collapse the line formation, while at $z = 120$ mm, the line formation of the proceeding bubbles is completely collapsed. Dispersion of the bubbles begins to occur in the z direction at $z > 120$ mm. The envelope of dispersed bubbles (i.e. bubble-swarm) has an oblate-ellipsoidal-like shape. In this phase, the bubbles behave as an organized cluster with a uniform void fraction

Profiles of the average vertical velocity components. Fig. 15(a)–(c) shows the profiles of the average vertical velocity component w of the frontal region at $z = 100$, 200, 300 mm, respectively; (d), (e), and (f) those of the rear region. A plateau-like pattern with a weak center peak is observed in the profiles of the frontal region. In contrast, in the profiles of the rear region, a clear center-peak pattern is observed. In addition, the maximum value in the rear region is 1.3–1.5 times larger than that

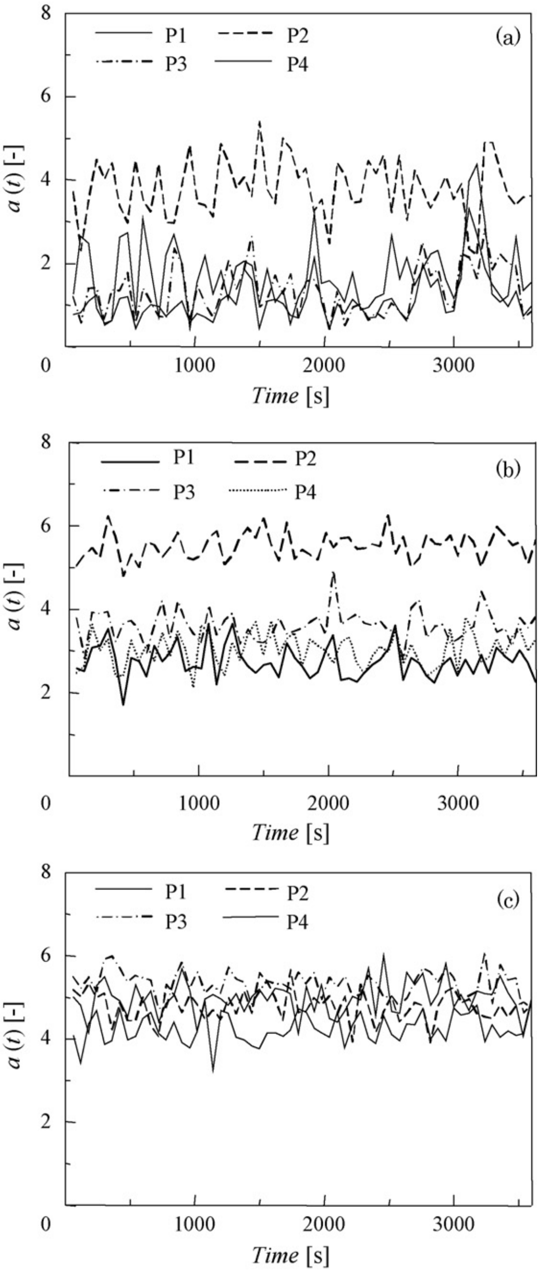

Fig. 17. Time-series void fraction obtained by four-point simultaneously measurement: (a) $z = 100$ mm, (b) $z = 700$ mm, (c) $z = 1300$ mm.

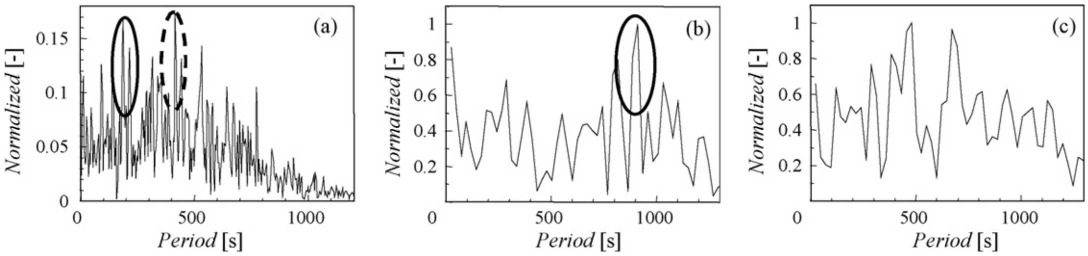

Fig. 18. Normalized spectra of pre-processed time-series void fraction: (a) integral time of 4 s at $z = 700$ mm; (b) 24 s at $z = 700$ mm; (c) 24 s at $z = 1900$ mm.

in the frontal region at the same position of z. Furthermore, width of the area where the average vertical velocity component has significant values is 1.5–1.8 times larger than width of single bubble-swarm. These results agree with that in frontal region at the same position of z. Although the dispersion of the bubbles develops with an ascent of the bubble-swarm, the analogy between a single bubble and the envelope bubble-swarm can be understood from the shape and velocity profiles [7]. Hence, in this phase, large-scale liquid-phase motion around the bubble-swarm (i.e. buoyancy-driven flow) is dominated by the envelope bubble-swarm that has a uniform void fraction in itself. In order to extract a large-scale structure (or long-period fluctuation) of a bubbly flow, our attention should be focused not on individual bubbles but on a bubble cluster. The bubble cluster should be an aggregation of point-wise areas with similar void fractions.

4.2. Characteristics of bubbly flow in a bubble column (statistical bubble properties in a bubble column)

Fig. 16 shows histograms of equivalent diameters and vertical velocity components of the bubbles. The distribution patterns of the equivalent diameter (i.e. distribution range and peak-value) at $z = 700$ mm and $z = 1300$ mm are the same. The frequencies take the peak-values at 4.4 mm and the major distribution range (95% data distributed) is 0.7–9.0 mm. In contrast, the distribution patterns at $z = 1900$ mm different from the others. Although the frequency takes the peak-value at almost 4 mm irrespective of z, the major distribution range at $z = 1900$ mm is 2.0–7.0 mm. In the upper region of the bubble column, the distribution range shifts to a lower value with regard to the bubble diameters. Furthermore, the vertical velocity components clearly shift to a lower value associated with an increase in height from the bottom. The distribution ranges of histograms became so broadly as to close in the bottom.

From the results of the flow visualization, we also determined that the flow regime changes with the height from the bottom. In the lower region, the flow is categorized as a heterogeneous flow, while in the upper region, the flow becomes homogeneous. As such, our results regarding the statistical distributions of equivalent bubble diameters and vertical velocity components directly reflect these flow regimes.

4.3. Long-period fluctuations in a bubble column

Spatial variation of time-series void fractions. The void fractions obtained simultaneously at four points [P1: $(x, y) = (-95$ mm, -95 mm), P2: $(x, y) = (-95$ mm, 95 mm), P3: $(x, y) = (95$ mm, 95 mm), P4: $(x, y) = (95$ mm, -95 mm)] are shown in Fig. 17. From these results, it is indirectly found that the void fractions are located eccentrically in space and that the magnitude of the fluctuation becomes large at $z = 700$ mm. The region of high void fractions moves in a circumferential direction with time. Although the magnitude of the fluctuation clearly decreases, the spatial variation of the void fraction remains at $z = 1300$ mm. In contrast, the spatial variation of the void fractions disappeared at $z = 1900$ mm. Furthermore, time-series void fractions have almost equal values at $z = 1900$ mm. Hence, the fluctuations of the void fractions fade out with height. These results are a good reflection of the flow regimes obtained by visualization

Cyclic quality of long-period fluctuations. A long-period fluctuation in a bubble column is generated by fluctuations of bubble clusters near the bottom of the bubble column. The long-period fluctuation of a large-scale bubble-swarm can be obtained by applying the newly proposed method. The dominant period is extracted via FFT analysis. Fig. 18 [(a): pre-processed with an integral time of 4 s at $(x, y, z) = (95$ mm, 95 mm, 100 mm); (b): with 24 s at $(x, y, z) = (95$ mm, 95 mm, 100 mm); (c) with 24 s at $(x, y, z) = (95$ mm, 95 mm, 1300 mm)] shows normalized spectra obtained from the pre-processed time-series point-wise void fractions. The spectrum shows peaks at periods of around 200 and 400 s in Fig. 18(a). Furthermore, at an integral time of 24 s [Fig. 18(b)], the spectrum shows a peak at a longer period of 900 s. Hence, the peak period becomes longer with increases in the integral time during pre-processing. Therefore, the integral time shall reflect the size of a characteristic bubble-swarm. Examples of the visualized images obtained at the lower region are shown in Fig. 19. Based on analysis of the time-series images of the targeted area (indicated by

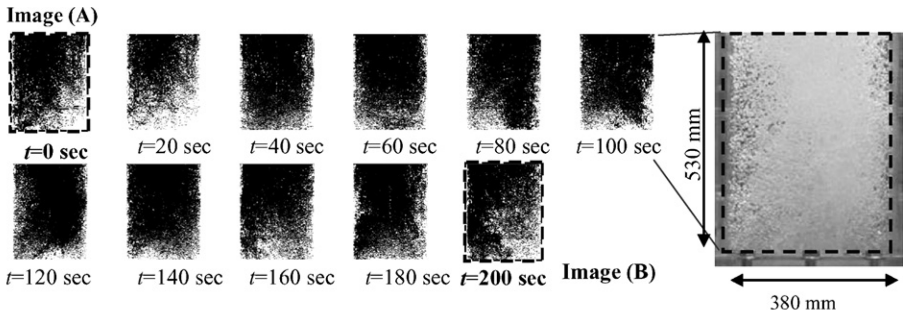

Fig. 19. Examples of visualized results (test section: 600 mm < $z \leq$ 1130 mm).

the red rectangle in Fig. 19), we observed a fluctuation period of approximately 200 s. This value corresponds well with the peak period obtained in Fig. 9(a). In contrast, in Fig. 8 [(c): $z = 1900$ mm], the spectrum has no dominant period. This difference between the spectrum patterns in Fig. 9(b) and (c) is a good reflection of the difference in the flow regimes.

5. Conclusions

The long-period fluctuations that reflect the large-scale structure of the buoyancy-driven flow in bubble columns are discussed. First, we considered a relationship between time-average and spatial-average point-wise void fractions. In our assumption of the relationship, the envelope bubble-swarm has a uniform void fraction. Furthermore, we thought that the space-average void fraction should be reflected in an integral time range, which shows a time-average sense of point-wise void fraction in the results of four-tip optical-fiber probe (F-TOP) measurement. Second, we demonstrated the analogy of the liquid-phase motion between the ascent of envelope bubble-swarm and single-bubble in detail. The liquid-phase flow structure induced by a controlled bubble-swarm (i.e. a bubble cluster with a uniform void fraction) was discussed by using LDA. The ascent of single bubble-swarm induced surrounding liquid-phase motion directly. In addition, the liquid-phase flow structure which is induced by single bubble-swarm had analogy to that of single bubble in perspectives of shape and liquid-phase velocity profiles. From these results, we explained the validity of our new method based on the F-TOP measurement which focuses to the motion of envelope bubble-swarm. Third, we measured the bubble characteristics in a bubble column 380 mm in inner diameter and 2100 mm in depth using F-TOP. The bubbly flows in the column were calcified into three regions (i.e. a time-spatially fluctuated region, a transition region, and a pseudo-homogenous region). Finally, we succeeded in extracting long-period fluctuations from FFT analysis of the pre-processed point-wise void fractions by using the newly developed method. The dominant periods were in good agreement with those obtained from the flow visualization. Furthermore, the characteristic spectra corresponding to each flow regime faded out with height from the column bottom. This result was in good agreement with the change in the flow regime.

References

[1] T. Saito, T. Kajishima, R. Nagaosa, CO_2 sequestration at sea by gas-lift system of shallow injection and deep releasing, Environ. Sci. Technol. 34 (2000) 4140–4145.
[2] T. Saito, S. Kosugi, T. Kajishima, Characteristics and performance of a deep-ocean disposal system for low-purity CO_2 gas via gas lift effect, Energy Fuels 15 (2001) 285–292.
[3] K. Akita, F. Yoshida, Gas holdup and volumetric mass transfer coefficient in bubble column, Ind. Eng. Chem. Process Des. Develop. 13 (1973) 84–91.
[4] K. Tsuchiya, T. Ishida, T. Saito, T. Kajishima, Dynamics of Interfacial Mass Transfer in a Gas-Dispersed System, Canadian Journal Chemical Engineering 81 (2003) 647–654.
[5] R.F. Mudde, Gravity driven bubbly flows, Annu. Rev. Fluid Mech. 37 (2005) 393–423.
[6] T. Saito, K. Tsuchiya, T. Kajishima, Local and global scale structure of bubbly flows in GLAD (gas lift advance dissolution) system, Exp. Therm. Fluid Sci. 29 (2005) 305–313.
[7] T. Saito, K. Sakakibara, Y. Miyamoto, M. Yamada, A study of surfactant effects on the liquid-phase motion around a zigzagging-ascent bubble using a recursive cross-correlation PIV, Chem. Eng. J. 158 (2010) 39–50.
[8] K. Morikawa, S. Urano, T. Sanada, T. Satio, Turbulence modulation induced by bubble swarm in oscillating-grid turbulence, J. Power Energy Syst. 2 (2008) 330–339.
[9] W.K. Harteveld1, R.F. Mudde, H.E.A. van den Akker, Dynamics of a bubble column: influence of gas distribution on coherent structures, Can. J. Chem. Eng. 81 (2003) 389–394.
[10] W. Warsito, L.S. Fan, Dynamics of spiral bubble plume motion in the entrance region of bubble columns and three-phase fluidized beds using 3DECT, Chem. Eng. Sci. 60 (2005) 6073–6084.
[11] B.J. Azzopardi, K. Jackson, J.P. Robinson, R. Kaji, M. Byars, A. Investigation of flow development of co-current gas–liquid vertical slug flow, Int. J. Multiphase Flow 35 (2009) 335–348.
[12] R.F. Mudde, T. Saito, Hydrodynamical similarities between bubble column and bubbly flow, J. Fluid Mech. 437 (2001) 203–228.
[13] T. Saito, M. Kitamura, T. Kajishima, H. Hatano, Measurement of bubble dynamics by an optical fibre probe (1st report), influence of an optical fibre probe on bubble interfacial motion, Trans. Jpn. Soc. Mech. Eng. Ser. B 65 (1999) 2619–2626 (in Japanese).
[14] L.S. Fan, K. Tsuchiya, Bubble Wake Dynamics in Liquids and Liquid–Solid Suspensions, vol. 437, Butterworth-Heinemann Series in Chemical Engineering, Reed Publishing Inc., USA, 1990.
[15] A. Brankovic, I.G. Currie, W.W. Martin, Laser Doppler measurements of bubble dynamics, Phys. Fluid 27 (1984) 348–355.